Available online at www.sciencedirect.com

jmr&t Journal of Materials Research and Technology

journal homepage: www.elsevier.com/locate/jmrt

Original Article

Tailoring microstructure of Ni_2CoFe medium-entropy alloy to achieve optimal comprehensive mechanical properties

Lei Gu [1], *Ningning Liang* [1], *Dongmei Zhang, Yong Fan, Jihua Liu, Yonghao Zhao* [*]

Nano and Heterogeneous Materials Center, School of Materials Science and Engineering, Nanjing University of Science and Technology, Nanjing 210094, China

ARTICLE INFO

Article history:
Received 14 December 2022
Accepted 10 February 2023
Available online 15 February 2023

Keywords:
Medium-entropy alloys
Microstructures
Strength and ductility
Cold-rolling
Annealing

ABSTRACT

Single-phase face-centered cubic (fcc) medium- and high-entropy alloys (MEAs/HEAs) have high ductility but low yield strength and hardness. In this work, the microstructures of single-phase fcc Ni_2CoFe MEAs were tuned via thermo-mechanical treatment (cold-rolling plus annealing). Microhardness and tensile tests revealed that the as-rolled Ni_2CoFe MEA had a high hardness of 331.2 HV and a high yield strength of 913 MPa but a poor fracture elongation of 7.9%, resulting from high-density lattice defects. With increasing annealing temperature, the hardness and strength gradually decreased and meanwhile the ductility gradually improved, due to the microstructural recovery, recrystallization and grain growth. The heterostructured sample annealed at 530 °C for 1 h exhibited simultaneous improvement in ultimate tensile strength and uniform elongation compared with those of as-rolled sample. For the heterostructured sample annealed at 550 °C for 1 h, a good fracture elongation of 13.6% and a decent ultimate tensile strength of 867 MPa were achieved. Extra hardening and strengthening were produced, benefiting from the construction of heterostructure. Moreover, the Ni_2CoFe MEA exhibited more superior combination of strength and ductility compared to pure Ni. The severe lattice distortion existing in the Ni_2CoFe MEA enhances the strain hardening and ductility by enhancing the dislocation accumulation capability.

1. Introduction

High-entropy alloys (HEAs), consisting of five or more multi-principal elements with equiatomic or near equiatomic composition, were invented by Ye et al. [1] and Cantor et al. [2] in 2004. Over the past decade, single-phase face-centered cubic (fcc) HEAs such as CrMnFeCoNi Cantor alloy and its derived medium-entropy alloy (MEAs) [3–7], body-centered

* Corresponding author.
E-mail address: yhzhao@njust.edu.cn (Y. Zhao).
[1] These authors contributed equally.
https://doi.org/10.1016/j.jmrt.2023.02.066

cubic (bcc) HEAs composed of refractory elements (Zr, Nb, Mo, Hf, Ta, W) [8–10], eutectic HEAs [11–15], and ordered phase strengthened HEAs [16,17], have been widely investigated. Currently, single-phase fcc HEAs/MEAs have high ductility but low strength and bcc refractory HEAs have high-temperature strength but low ductility at room temperature. Besides, a variety of excellent performances, for instance, high hardness [18–20], extremely low coercivity [21], outstanding irradiation resistance [22,23] and wear resistance [24,25], have been found in the multisystem HEAs/MEAs. Owing to these exciting properties, HEAs/MEAs have attracted extensive attention of materials researchers.

For single-phase fcc HEAs/MEAs, the yield strength (YS) can be effectively improved by introducing a large number of lattice defects, including dislocations and grain boundaries (GBs) [26]. Cold-rolling is an economical and effective method to obtain bulk ultrafine-grained (UFG) materials with grain size smaller than 1 μm. Inevitably, the strain hardening capacity and tensile ductility would be reduced, analogous to conventional alloys [27–30]. This classical phenomenon is known as strength-ductility trade-off. Normally, subsequent annealing on severely deformed materials is an uncomplicated method to achieve the controllable and desired combination of strength and ductility. However, most HEAs/MEAs are unstable and easy to produce second-phase during heat treatment at medium temperature, resulting from their high mixing enthalpy. Gu et al. [31] reported that long-range ordered structure formed in the stable single-phase Cantor alloy after annealing treatment at 500 °C and then induced the abnormal hardening and severe brittleness. Furthermore, Zhang et al. [32] found that topological close-packed phase (TCP) σ-phase formed in the cold-rolled $Co_{34.5}Cr_{30}Ni_{26.5}Al_{5.4}W_{3.6}$ HEA after annealing at 800 °C–900 °C. Likewise, the $(CoCrFeNi)_{(100-x-6)}(WMo)_x(AlTi)_6$ (x = 1, 3, 5) HEAs also produced the submicron σ phase, nano γ′ phase and micron (Ti, W, Mo)-rich phase after aging at 700 °C or 650 °C [33]. These precipitated phases, especially for TCP phases, are hard to deform and even brittle. Although the strength can be enhanced substantially by these second-phases, the tensile ductility may be destroyed disastrously. Moreover, the size and morphology of the precipitates also affect the strength-ductility trade-off. The large-sized precipitated phases in HEAs result in the severe reduction of ductility [34]. Therefore, the phase stability at medium temperature is significant for tailoring the synergy of strength and ductility.

In recent years, based on the regulation of microstructure, heterostructured materials, composed of heterogeneous zones with dramatically different (>100%) mechanical or physical properties, are well-designed [35]. An additional synergistic effect between heterogeneous zones contributes to excellent mechanical or physical properties, surpassing the evaluated properties by the rule of mixture [35]. For heterostructured metallic materials, extra hetero-deformation induced (HDI) strengthening and hardening are conducive to the superior mechanical properties [36–38]. It is attributed to more geometrically necessary dislocations (GNDs) pile-ups at the interfaces of soft/hard zones, providing the additional HDI stress. Therefore, introducing heterogeneous grain structure in single-phase fcc HEAs/MEAs can obtain the unexpected combination of strength and ductility.

In this work, the microstructures of single-phase fcc Ni_2CoFe MEAs were tuned by cold-rolling combined with subsequent partial or full recrystallization annealing. The microstructural evolutions of the cold-rolled and annealed samples were investigated by electron backscattered diffraction (EBSD) characterization in details. Finally, the microhardness and tensile behaviors of all thermo-mechanically treated samples were tested.

2. Experiments

2.1. Sample preparation

The MEA ingots with a nominal chemical composition Ni_2CoFe (in at.%) were prepared by arc-melting a mixture of commercial metals (Purity >99.9%). The ingots were re-melted at least four times to improve composition homogeneity. The as-cast MEAs were cut into plates and then were cold-rolled with the thickness reduction of ~90% at room temperature (labeled as CR90 sample). Specimens cut from the cold-rolled sheet were isochronally annealed at temperatures ranging from 500 °C to 900 °C for 1 h under Ar atmosphere (labeled as A500 - A900 samples).

2.2. Mechanical testing

The tensile tests were performed on a LTM-20KN testing machine with a constant strain rate of $1 \times 10^{-3}\ s^{-1}$ at ambient temperature. Flat dog-bone-shaped tensile specimens with gauge dimensions of $10 \times 2.5 \times 1.5\ mm^3$ were electro-discharge machined from the cold-rolled and as-annealed specimen sheets. At least three tensile specimens were tested for each sample to obtain repeatable experimental results. The Vickers hardness was characterized on SHIMADZU HMV-G21 tester with a load of 4.9 N for 15s and at least ten randomly indentations were tested to obtain a mean value.

2.3. Microstructure characterizations

Microstructural evolutions of the cold-rolled Ni_2CoFe MEAs after annealing were characterized by scanning electron microscopy equipped with EBSD detectors. The EBSD specimens were mechanically polished first and then followed by electro-polishing using an electrolyte consisting of 90 vol% acetic acid and 10 vol% perchloric acid with a voltage of 35 V at room temperature. EBSD measurements were performed on an Oxford Instruments Aztec system and the quantitative analyses were implemented using a commercial channel 5 software. The scanning step size was chosen as 0.5 μm for all samples. X-ray diffraction (XRD) were performed by Bruker-AXS D8 with the angle of 2θ scanning from 30° to 90° and a scanning speed of $2°\ min^{-1}$. The specimens for transmission electron microscopy (TEM) observation were electro-polished in a twin jet electro-polishing system containing an electrolyte consisting of 10% perchloric acid, 20% glycerol and 70%

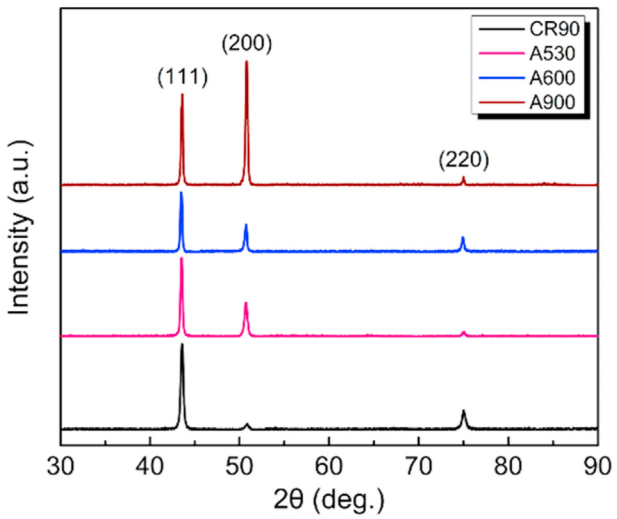

Fig. 1 – XRD patterns of the as-rolled and subsequently annealed Ni_2CoFe MEAs.

methanol at −20 °C, and then observed by an FEI-Tecnai G^2 20 S-TWIN microscope operating at 200 kV.

3. Results and discussion

The CR90 sample exhibits a single-phase fcc structure with a very strong (111) peak and a weak (200) peak along normal direction, as shown from the XRD patterns in Fig. 1. After annealing at medium temperatures (530 °C and 600 °C), no second-phase formed and the Ni_2CoFe MEA still had a stable single-phase fcc structure. The relative intensity of (200) peaks of A530 and A600 samples increased, indicating that the rolling textures changed and a small minority of recrystallization textures existed. With increasing the annealing temperature to 900 °C, the peak intensity of (200) increases significantly.

The microstructures of the CR90 sample are shown in Fig. 2. The CR90 sample is composed of elongated sub-millimeter-sized grains along rolling direction (which are separated by dashed lines) and plenty of randomly oriented fine grains formed by dynamic recrystallization during cold-rolling processing (Fig. 2a). These elongated sub-millimeter-sized grains evolved from the as-cast sample, which consists of coarse grains with several hundreds of micrometers, as shown in our previous work [24]. Low-angle GBs (LAGBs, 2°–15°) and high-angle GBs (HAGBs, >15°) are marked by yellow and black lines in Fig. 2b, respectively. The LAGBs are found throughout the whole CR90 sample and the volume fraction reaches up to ~91%. From the bright-field TEM image, the CR90 sample consists of ultrafine lamellar sub-grains with an average thickness of ~130 nm, in which there are high-density dislocations (Fig. 2c). No deformation twin formed during cold-rolling (Fig. 2c), further verified by EBSD result. As shown in Fig. 2d, there is no peak of 60° twin boundaries (TBs). This is because the Ni_2CoFe MEA has a high stacking fault energy (SFE), which deform plastically via dislocation slip instead of mechanical twinning. As reported in the literature

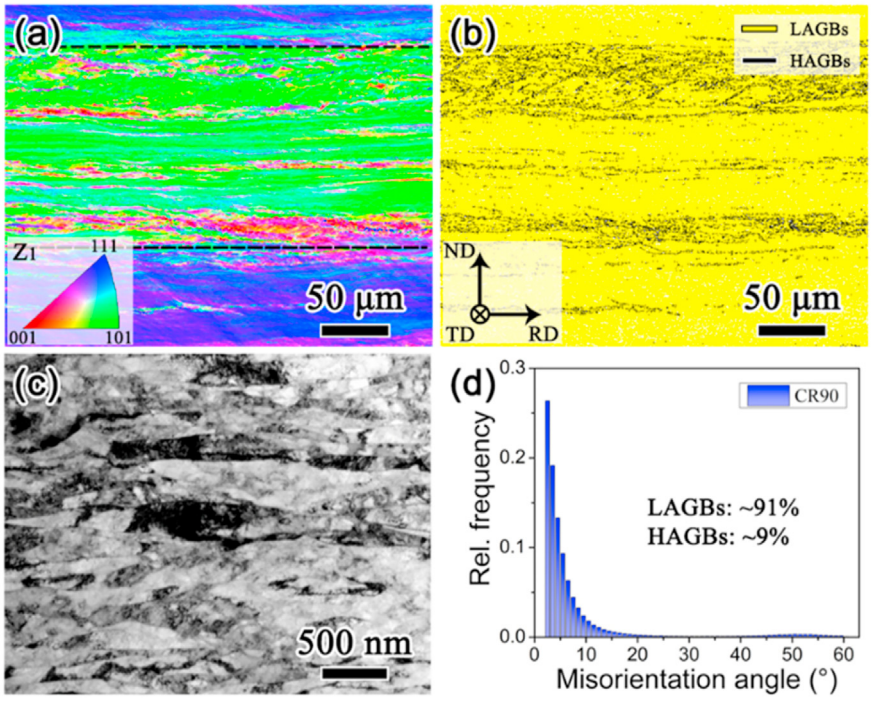

Fig. 2 – The microstructures of the cold-rolled Ni_2CoFe MEA. (a) EBSD crystal orientation map with IPF color code of Z_1//TD. RD: rolling direction; TD: transverse direction; ND: normal direction. (b) Grain boundary (GB) map with low- and high-angle GBs (LAGBs: 2°–15°, HAGBs: >15°) marked by yellow and black lines, respectively. (c) Bright-field TEM image from RD-ND plane. (d) The distribution of GB misorientation angle.

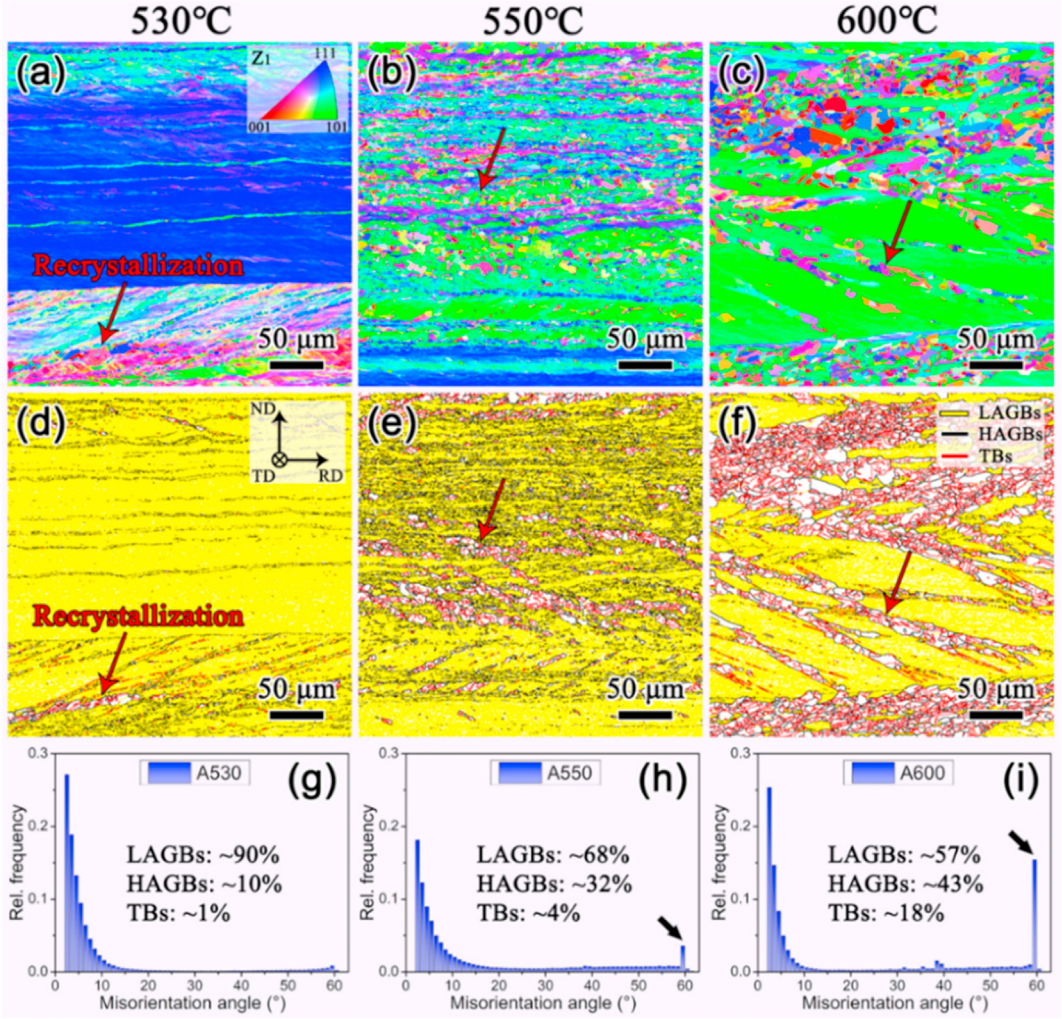

Fig. 3 – EBSD crystal orientation and GB maps of partially-recrystallized Ni_2CoFe MEAs: (a, d) A530; (b, e) A550 and (c, f) A600. The LAGBs, HAGBs and twin boundaries (TBs: 60°) are marked by yellow, black and red lines in (d–f), respectively. The corresponding distributions of GB misorientation angle of (g) A530, (h) A550 and (i) A600 samples. The recrystallized zones are pointed by red arrows in (a–f).

[39], the $Ni_2CoCrFe$ alloy had a reduced SFE due to the heavy addition of Cr element, but still deformed through dislocation glide, bringing about the formation of dislocation cells and high dense dislocation walls during tensile testing. With further decreasing the content of Ni element, the SFE of NiCoCrFe HEA reduced to ~32.5 mJ m^{-2} at 293 K and deformation twinning was activated at room temperature [40]. For Cantor alloy with a lower SFE (~25 mJ m^{-2}) [41], high-density intersected deformation twins were produced by asymmetric rolling [42].

After annealing at 530 °C–600 °C for 1 h, the as-rolled samples were partially recrystallized (Fig. 3). The A530, A550 and A600 samples are all composed of non-recrystallized grains (NRGs) and recrystallized equiaxed micro-grains (marked by red arrows). With increasing annealing temperature, the recrystallization fraction increased from 2.1% of A530 to 26.6% of A550, then to 50.6% of A600. Fig. 3d–f shows the GB map with LAGBs, HAGBs and Σ3 coincident-site lattice TBs (marked by red lines). In the recrystallized grains (RGs), there are almost no LAGBs but plentiful annealing twins, resulting from dislocations migration, rearrangement, and annihilation during annealing. Moreover, RGs in the A600 sample have the lager average grain size (Fig. 3f) compared with the A550 sample (Fig. 3e), which are respectively ~5.4 μm and ~3.2 μm, indicating grain growth occurred in recrystallization zone during annealing at relatively high temperature. The corresponding distributions of GB misorientation angle of A530, A550 and A600 samples are shown in Fig. 3g–i, respectively. The A530 sample still has a large amount of LAGBs with the volume fraction of ~90%, close to the CR90 sample (~91%). For the A550 and A600 samples, the visible peaks of 60° TBs can be found, which are annealing TBs (marked by black arrows in Fig. 3h–i). The volume fraction of TBs are 4% of A550 sample and 18% of A600 sample, respectively. TEM observation focusing on A600 sample was further performed in order to supplement EBSD information, as shown in Fig. 4. The

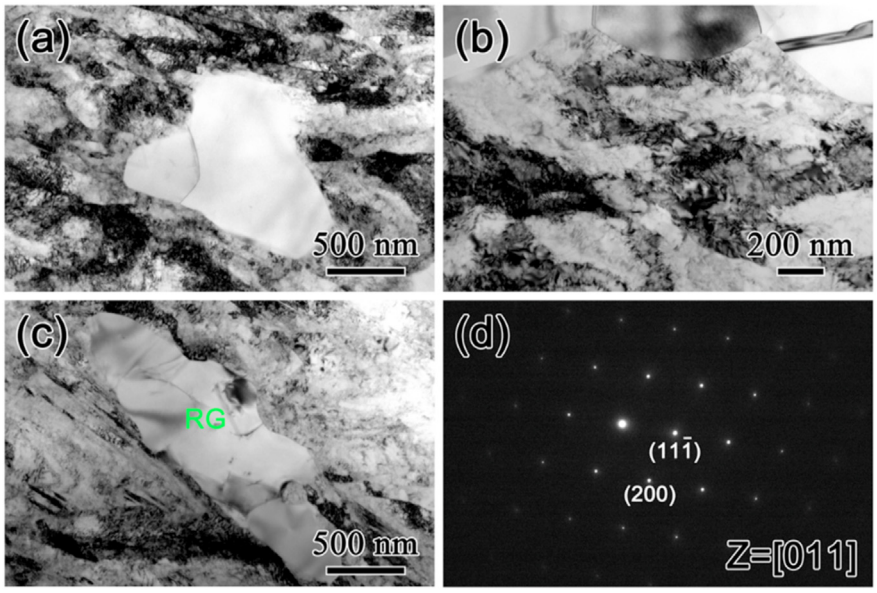

Fig. 4 – (a–c) Bright field TEM images of partially-recrystallized Ni_2CoFe MEA after annealing at 600 °C for 1 h. (d) The selected area electron diffraction pattern of the recrystallized grain (RG) in (c).

equiaxed RGs have a very low dislocation density and are surrounded by NRGs which have high-density dislocations. No second phase or precipitated particle can be found. The single-phase fcc structure is further verified by selected area electron diffraction pattern in Fig. 4d.

The local misorientation maps and corresponding Kernel average misorientation (KAM) value distributions of A530, A550 and A600 Ni_2CoFe samples are shown in Fig. 5. The rainbow color bar from blue to red represents the local misorientation from low to high, indicating low-to high-density GNDs. The recrystallized zones (marked by red arrows) have lower GNDs densities and the non-recrystallized zones have higher stored strain energy (Fig. 5a–c). The KAM values of all three samples exhibit a bimodal distribution with the

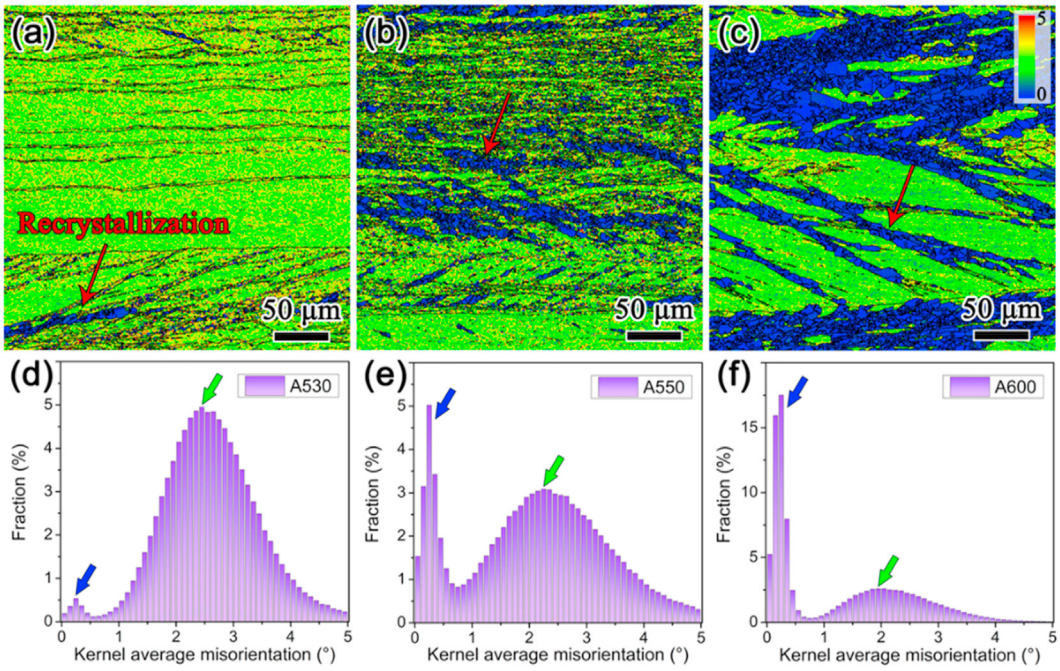

Fig. 5 – The local misorientation maps and corresponding Kernel average misorientation (KAM) value distributions of (a, d) A530; (b, e) A550 and (c, f) A600 Ni_2CoFe MEAs. The inset in (c) is the rainbow color bar (blue to red represent low to high misorientation). The recrystallized zones are pointed by red arrows in (a–c). The KAM peaks of recrystallized and non-recrystallized zones are marked by blue and green arrows in (d–f), respectively.

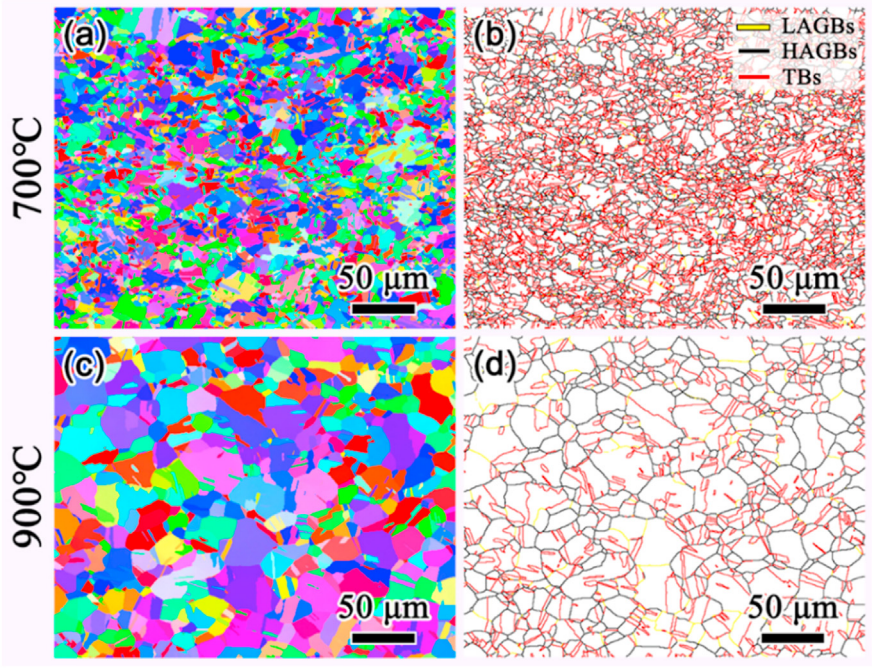

Fig. 6 – EBSD crystal orientation and GB maps of fully-recrystallized Ni_2CoFe MEAs: (a, b) A700 and (c, d) A900. The LAGBs, HAGBs and 60° TBs are marked by yellow, black and red lines in (b, d), respectively.

peaks of recrystallized (marked by blue arrows) and non-recrystallized zones (marked by green arrows), as shown in Fig. 5d–f. The A600 sample has relatively lower dislocation densities in the non-recrystallized zones compared with the A530 and A550 samples. It also can be quantificationally verified that the KAM peak of non-recrystallized zones in the A600 sample shifts to the left (Fig. 5f), indicating plenty of GNDs recovered when annealing at 600 °C. The average KAM values of A530, A550 and A600 samples are 2.58°, 1.92° and 1.25°, respectively. The GNDs density has linear relation with

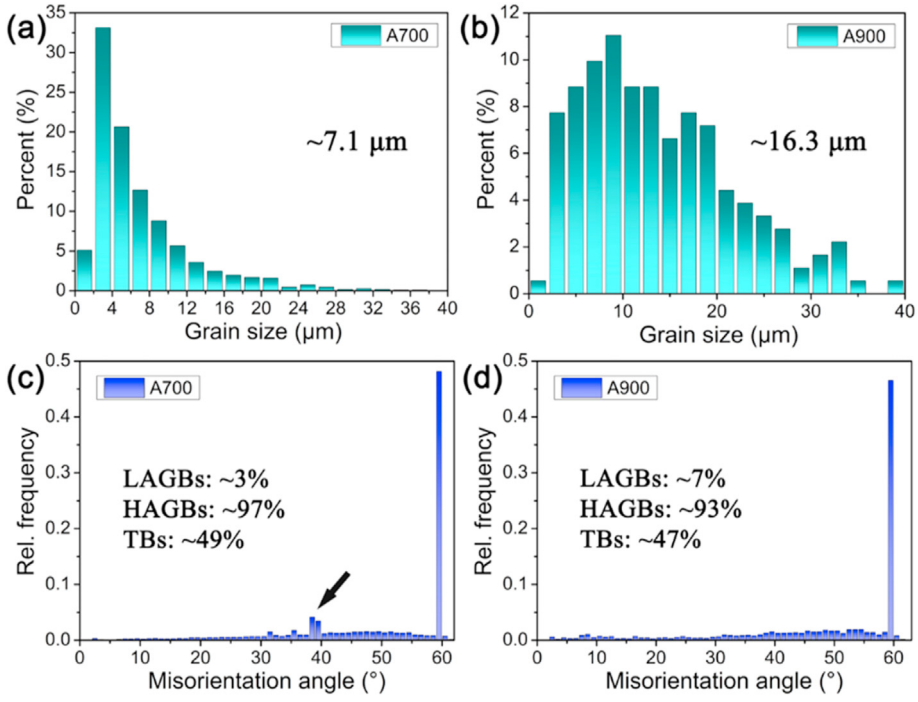

Fig. 7 – Distributions of grain size and GB misorientation angle of fully-recrystallized Ni_2CoFe MEAs: (a, c) A700 and (b, d) A900.

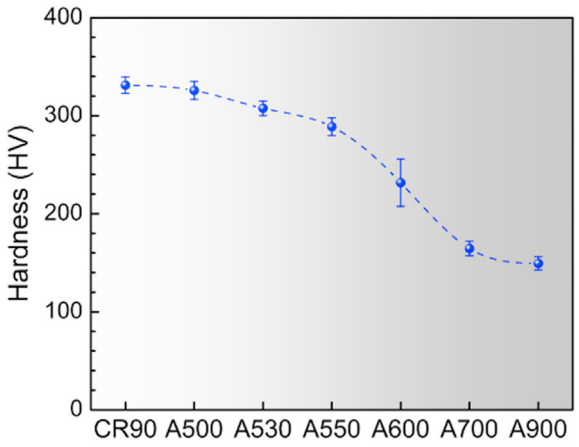

Fig. 8 – Microhardness evolution of as-rolled Ni_2CoFe MEAs after isochronally annealing for 1 h.

the average KAM value and can be calculated by the formula from the strain gradient theory by Gao [43] and Kubin [44]:

$$\rho = \frac{\theta^{KAM}}{ub}$$

where ρ is the density of GNDs; u is the step size, which is 0.5 μm, used in EBSD acquisition; b is the Burgers vector (0.252 nm in use, $b = \frac{\sqrt{2}a}{2}$, a = 0.356 nm calculated from XRD results); θ^{KAM} is the averaged KAM value. The calculated GNDs densities are 3.6×10^{14} m^{-2} for A530, 2.7×10^{14} m^{-2} for A550 and 1.7×10^{14} m^{-2} for A600 samples.

After annealing at 700 °C and 900 °C for 1 h, the as-rolled samples were fully recrystallized (Fig. 6). Both A700 and A900 samples consist of randomly oriented equiaxed micron-sized grains. Almost uniform color distribution in individual grain interior shows no change of interior misorientation and low density of dislocations. Both samples have a high density of annealing twins (red lines) inside the RGs, as shown in Fig. 6b and d. The corresponding distributions of grain size and GB misorientation angle are shown in Fig. 7. The A700 and A900 samples have the averaged grain sizes of 7.1 μm and 16.3 μm (excluding annealing twins), respectively. The A700 sample has ~97% HAGBs and ~49% TBs. In contrast, the A900 sample has the reduced HAGBs fraction of ~93% and TBs fraction of ~47%. With further annealing, the proportion of LAGBs slightly increased due to the lower GB energy. Moreover, the A700 sample shows a strong peak at ~39° (marked by black arrow in Fig. 7c), which corresponds to Σ9 annealing TBs with 38.9° <110> misorientation [45]. This strong Σ9 peak also can be found in the A600 sample (Fig. 3i) but becomes weakened in the A900 sample (Fig. 7d), indicating its instability at high temperature.

The measured microhardness of thermo-mechanical treated Ni_2CoFe MEAs are plotted in Fig. 8. In general, the hardness decreased monotonously with the increasing annealing temperature, as listed in Table 1. The CR90 sample has an average hardness of 331.2 HV. After annealing at 500 °C for 1 h, the hardness value barely changed and only decreased to 325.8 HV, which may be attributed to the recovery of a small number of lattice defects. Further increasing annealing temperature to 530 °C, the hardness slightly decreased to 307.5 HV, resulting from the partial recrystallization (Fig. 5a). Notably, the A600 sample exhibits extremely fluctuating hardness values and has a mean value of 231.7 HV, due to the existence of ~50 vol% hard NRGs and ~50 vol% soft RGs. Annealing induced softening is universal at high temperature derived from recrystallization and grain growth. The fully-recrystallized A700 and A900 samples have the averaged hardness of 164.5 and 149.3 HV, respectively. On the contrary, annealing induced hardening was usually found in severely deformed HEAs/MEAs especially annealing at medium temperatures [46,47]. Liang et al. [46] found that annealing induced hardening occurred below 600 °C in a nanocrystalline $FeNi_2CoMo_{0.2}V_{0.5}$ HEA without precipitated phase, derived from the sustained deformation twin barriers and annihilation of mobile dislocations. Commonly, the formation of precipitated phases during medium-temperature annealing would pin dislocations and GBs, thereby causing hardening [48].

The representative engineering stress-strain curves of thermo-mechanical treated Ni_2CoFe MEAs are compared in Fig. 9a. The CR90 sample exhibits a high YS of 913 MPa but a poor fracture elongation of 7.9%. Besides, there is almost no uniform elongation (1.6%) and necking occurred instantly after yielding. High-density LAGBs and dislocations in the CR90 sample contributed to the high YS but led to the inferior dislocation storage capability. After annealing at 500 °C for 1 h, the tensile behavior remained almost unchanged. Further elevating annealing temperature, the uniform and fracture elongations gradually improved but at the same time the YS and ultimate tensile strength (UTS) gradually decreased (Fig. 9b), derived from the microstructural recovery, recrystallization and grain growth. The A550 sample composed of 26.6 vol% RGs has a good fracture elongation of 13.6% and a decent UTS of 867 MPa. On the basis of the rule of mixture, the YS of A550 sample was estimated to be ~740 MPa based on the YSs of A500 and A700 samples with 900 MPa and 288 MPa, slightly lower than the experimental value of 776 MPa. It means that extra HDI strengthening was produced by the synergistic effect of hard (NRGs) and soft (RGs) zones. Likewise, Wu et al.

Table 1 – Lists of yield strength (YS), ultimate tensile strength (UTS), uniform elongation ε_{ue}, elongation to failure ε_{ef} and microhardness of Ni_2CoFe MEAs after thermo-mechanical treatments with different conditions.

Samples	CR90	A500	A530	A550	A600	A700	A900
YS, MPa	913	900	880	776	519	288	214
UTS, MPa	914	908	917	867	706	577	537
ε_{ue}, %	1.6	1.8	3.9	7.2	15.3	31.7	38.5
ε_{ef}, %	7.9	7.2	8.8	13.6	22.9	40.7	53.4
Hardness, HV	331.2	325.8	307.5	288.8	231.7	164.5	149.3

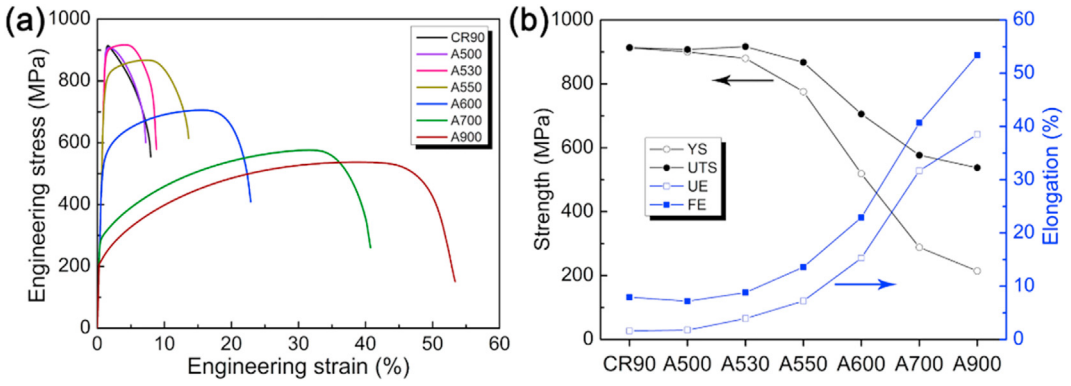

Fig. 9 – Tensile properties of Ni_2CoFe MEAs after thermo-mechanical treatments with different conditions. (a) Engineering stress-strain curves. (b) Evolution of yield strength (YS), ultimate tensile strength (UTS), uniform elongation (UE) and elongation to fracture (FE).

[49] reported that heterostructured Ti samples containing over 20% softer recrystallized lamellae were as strong as the UFG Ti. They found that back stresses in softer zones were conducive to the high strength [49]. For the A900 sample, the YS and UTS reduced to 214 MPa and 537 MPa, respectively, and the elongation to fracture increased to 53.4%. Nevertheless, the A900 Ni_2CoFe MEA exhibits more superior combination of strength and ductility compared to the coarse-grained (CG) pure Ni [36]. This is because the Ni_2CoFe MEA is concentrated solid solution and has more severe lattice distortion compared with pure Ni. The resistance of dislocation slip could be enhanced by chemical short-range order [50,51], thus maximizing the solid-solution strengthening effect in HEAs/MEAs.

4. Conclusions

In summary, the microstructures of the stable single-phase fcc Ni_2CoFe MEAs were tailored by low-cost and high-efficiency method combined cold-rolling with annealing and then their mechanical properties were tested. High-density dislocations in the UFG CR90 Ni_2CoFe MEA contributed to a high hardness of 331.2 HV and a high YS of 913 MPa. Inevitably, the tensile ductility of CR90 sample was sacrificed because of the inferior dislocation storage capability. With the microstructural recovery, recrystallization and grain growth during annealing, the hardness and tensile strength gradually decreased and meanwhile the tensile ductility gradually improved. The heterostructured A530 sample exhibited simultaneous improvement in ultimate tensile strength and uniform elongation compared with those of as-rolled sample, which increased from 914 to 917 MPa and from 1.6% to 3.9%, respectively. For the heterostructured A550 Ni_2CoFe MEA containing 26.6 vol% RGs, a good fracture elongation of 13.6% and a decent UTS of 867 MPa were achieved. Based on the rule of mixture, the YS of A550 sample was estimated to be ~740 MPa slightly lower than the experimental value of 776 MPa, indicating extra HDI strengthening was produced by the synergistic effect of hard (NRGs) and soft (RGs) zones. Moreover, the CG A900 Ni_2CoFe MEA exhibited more superior strength and ductility synergy with a YS of 214 MPa and a fracture elongation of 53.4%, compared to the CG pure Ni. This is due to severe lattice distortion existing in the Ni_2CoFe MEA, which can be conducive to enhance the resistance of dislocation slip.

Declaration of competing interest

The authors declare that they have no known competing financial interests or personal relationships that could have appeared to influence the work reported in this paper.

Acknowledgements

The authors acknowledge financial supports from the National Key R&D Program of China (Grant No. 2021YFA1200203), National Natural Science Foundation of China (Grant No. 51971112, 51225102, 52105368), Natural Science Foundation of Jiangsu Province, China (Grant No. BK20190478) and the Fundamental Research Funds for the Central Universities (Grant No. 30919011405). The authors also want to acknowledge the support of the Jiangsu Key Laboratory of Advanced Micro-Nano Materials and Technology. TEM and EBSD experiments were performed at Center of Analytical Facilities Nanjing University of Science and Technology.

REFERENCES

[1] Yeh JW, Chen SK, Lin SJ, Gan JY, Chin TS, Shun TT, et al. Nanostructured high-entropy alloys with multiple principal elements: novel alloy design concepts and outcomes. Adv Eng Mater 2004;6:299–303.
[2] Cantor B, Chang ITH, Knight P, Vincent AJB. Microstructural development in equiatomic multicomponent alloys. Mater Sci Eng, A 2004;375–377:213–8.
[3] Gludovatz B, Hohenwarter A, Catoor D, Chang EH, George EP, Ritchie RO. A fracture-resistant high-entropy alloy for cryogenic applications. Science 2014;345:1153–7.
[4] Li Z, Pradeep KG, Deng Y, Raabe D, Tasan CC. Metastable high-entropy dual-phase alloys overcome the strength-ductility trade-off. Nature 2016;534:227–30.

[5] Jiang W, Gao X, Cao Y, Liu Y, Mao Q, Gu L, et al. Charpy impact behavior and deformation mechanisms of $Cr_{26}Mn_{20}Fe_{20}Co_{20}Ni_{14}$ high-entropy alloy at ambient and cryogenic temperatures. Mater Sci Eng, A 2022;837:142735.
[6] Jiang W, Gao X, Guo Y, Chen X, Zhao Y. Dynamic impact behavior and deformation mechanisms of $Cr_{26}Mn_{20}Fe_{20}Co_{20}Ni_{14}$ high-entropy alloy. Mater Sci Eng, A 2021;824:141858.
[7] Wang L, Liu B, Zhou J, Cao Y, Zhang F, Zhao Y. Unconventional dislocation starvation behavior of medium-entropy alloy single crystal pillars containing pre-existing dislocations. J Mater Sci Technol 2023;142:60–75.
[8] Lei Z, Liu X, Wu Y, Wang H, Jiang S, Wang S, et al. Enhanced strength and ductility in a high-entropy alloy via ordered oxygen complexes. Nature 2018;563:546–50.
[9] Wang F, Balbus GH, Xu S, Su Y, Shin J, Rottmann PF, et al. Multiplicity of dislocation pathways in a refractory multiprincipal element alloy. Science 2020;370:95–101.
[10] Wei S, Kim SJ, Kang J, Zhang Y, Zhang Y, Furuhara T, et al. Natural-mixing guided design of refractory high-entropy alloys with as-cast tensile ductility. Nat Mater 2020;19:1175–81.
[11] Lu Y, Gao X, Jiang L, Chen Z, Wang T, Jie J, et al. Directly cast bulk eutectic and near-eutectic high entropy alloys with balanced strength and ductility in a wide temperature range. Acta Mater 2017;124:143–50.
[12] Gao X, Lu Y, Zhang B, Liang N, Wu G, Sha G, et al. Microstructural origins of high strength and high ductility in an $AlCoCrFeNi_{2.1}$ eutectic high-entropy alloy. Acta Mater 2017;141:59–66.
[13] Shi P, Li R, Li Y, Wen Y, Zhong Y, Ren W, et al. Hierarchical crack buffering triples ductility in eutectic herringbone high-entropy alloys. Science 2021;373:912–8.
[14] Ren J, Zhang Y, Zhao D, Chen Y, Guan S, Liu Y, et al. Strong yet ductile nanolamellar high-entropy alloys by additive manufacturing. Nature 2022;608:62–8.
[15] Wu H, Xie J, Yang H, Shu D, Hou G, Li J, et al. A cost-effective eutectic high entropy alloy with an excellent strength-ductility combination designed by VEC criterion. J Mater Res Technol 2022;19:1759–65.
[16] Yang T, Zhao YL, Tong Y, Jiao ZB, Wei J, Cai JX, et al. Multicomponent intermetallic nanoparticles and superb mechanical behaviors of complex alloys. Science 2018;362:933–7.
[17] Yang Y, Chen T, Tan L, Poplawsky JD, An K, Wang Y, et al. Bifunctional nanoprecipitates strengthen and ductilize a medium-entropy alloy. Nature 2021;595:245–9.
[18] Gu L, Liang N, Liu Y, Chen Y, Liu J, Sun Y, et al. Novel as-cast NiAlCoFeNb dual-phase high-entropy alloys with high hardness. Mater Lett 2022;324:132676.
[19] Tang T, Wan N, Shen M, Jiao H, Liu D, Tang X, et al. A comparison of the microstructures and hardness values of non-equiatomic (FeNiCo)-(AlCrSiTi) high entropy alloys having thermal histories related to laser direct metal deposition or vacuum remelting. J Mater Res Technol 2021;15:696–707.
[20] Edalati P, Mohammadi A, Ketabchi M, Edalati K. Ultrahigh hardness in nanostructured dual-phase high-entropy alloy AlCrFeCoNiNb developed by high-pressure torsion. J Alloys Compd 2021;884:161101.
[21] Han L, Maccari F, Filho IRS, Peter NJ, Wei Y, Gault B, et al. A mechanically strong and ductile soft magnet with extremely low coercivity. Nature 2022;608:310–6.
[22] Lu Y, Huang H, Gao X, Ren C, Gao J, Zhang H, et al. A promising new class of irradiation tolerant materials: $Ti_2ZrHfV_{0.5}Mo_{0.2}$ high-entropy alloy. J Mater Sci Technol 2019;35:369–73.
[23] El-Atwani O, Li N, Li M, Devaraj A, Baldwin JKS, Schneider MM, et al. Outstanding radiation resistance of tungsten-based high-entropy alloys. Sci Adv 2019;5:eaav2002.
[24] Meng A, Liang F, Gu L, Mao Q, Zhang Y, Chen X, et al. An exceptionally wear-resistant $CoFeNi_2$ medium entropy alloy via tribo-induced nanocrystallites with amorphous boundaries. Appl Surf Sci 2023;614:156102.
[25] An XL, Liu ZD, Zhang LT, Zou Y, Xu XJ, Chu CL, et al. A new strong pearlitic multi-principal element alloy to withstand wear at elevated temperatures. Acta Mater 2022;227:117700.
[26] Jiang W, Zhu Y, Zhao Y. Mechanical properties and deformation mechanisms of heterostructured high-entropy and medium-entropy alloys: a review. Front Mater 2022;8:792359.
[27] Sathiyamoorthi P, Kim HS. High-entropy alloys with heterogeneous microstructure: processing and mechanical properties. Prog Mater Sci 2022;123:100709.
[28] Cao Y, Ni S, Liao XZ, Song M, Zhu YT. Structural evolutions of metallic materials processed by severe plastic deformation. Mater Sci Eng R 2018;133:1–59.
[29] Mao Q, Liu Y, Zhao Y. A review on mechanical properties and microstructure of ultrafine grained metals and alloys processed by rotary swaging. J Alloys Compd 2022;896:163122.
[30] Gu L, Liang N, Chen Y, Zhao Y. Achieving maximum strength-ductility combination in fine-grained Cu-Zn alloy via detwinning and twinning deformation mechanisms. J Alloys Compd 2022;906:164401.
[31] Gu J, Song M. Annealing-induced abnormal hardening in a cold rolled CrMnFeCoNi high entropy alloy. Scripta Mater 2019;162:345–9.
[32] Zhang L, Zhang L, Wang H, Li J, Man J, Xu Z, et al. Evolution of the microstructure and mechanical properties of an sigma-hardened high-entropy alloy at different annealing temperatures. Mater Sci Eng, A 2022;831:142140.
[33] Man J, Wu B, Duan G, Zhang L, Wan G, Zhang L, et al. Annealing-induced abnormal hardening in a cold rolled CrMnFeCoNi high entropy alloy. J Alloys Compd 2022;902:163774.
[34] Liu L, Zhang Y, Han J, Wang X, Jiang W, Liu CT, et al. Nanoprecipitate-strengthened high-entropy alloys. Adv Sci 2021;8:2100870.
[35] Zhu YT, Ameyama K, Anderson PM, Beyerlein IJ, Gao HJ, Kim HS, et al. Heterostructured materials: superior properties from hetero-zone interaction. Mater Res Lett 2021;9:1–31.
[36] Liu Y, Cao Y, Mao Q, Zhou H, Zhao Y, Jiang W, et al. Critical microstructures and defects in heterostructured materials and their effects on mechanical properties. Acta Mater 2020;189:129–44.
[37] Sun X, Hao X, Nie J, Fan Y, Chen Y, Liu S, et al. Microstructure and enhanced cryogenic tensile property of a heterostructured Al-AlN/Al-Mg composite fabricated by accumulative roll bonding (ARB). J Mater Res Technol 2022;21:532–45.
[38] Gao B, Lai Q, Cao Y, Hu R, Xiao L, Pan Z, et al. Ultrastrong low-carbon nanosteel produced by heterostructure and interstitial mediated warm rolling. Sci Adv 2020;6:eaba8169.
[39] He F, Wei S, Cann JL, Wang Z, Wang J, Tasan CC. Composition-dependent slip planarity in mechanically-stable face centered cubic complex concentrated alloys and its mechanical effects. Acta Mater 2021;220:117314.
[40] Wang Y, Liu B, Yan K, Wang M, Kabra S, Chiu Y, et al. Probing deformation mechanisms of a FeCoCrNi high-entropy alloy at 293 and 77 K using in situ neutron diffraction. Acta Mater 2018;154:79–89.
[41] Zaddach AJ, Niu C, Koch CC, Irving DL. Mechanical properties and stacking fault energies of NiFeCrCoMn high-entropy alloy. JOM 2013;65:1780–9.

[42] Han ZH, Liang S, Yang J, Wei R, Zhang CJ. A superior combination of strength-ductility in CoCrFeNiMn high-entropy alloy induced by asymmetric rolling and subsequent annealing treatment. Mater Charact 2018;145:619–26.
[43] Gao H, Huang Y. Mechanism-based strain gradient plasticity-I. Theory. J Mech Phys Solid 1999;47:1239–63.
[44] Kubin LP, Mortensen A. Geometrically necessary dislocations and strain-gradient plasticity: a few critical issues. Scripta Mater 2003;48:119–25.
[45] Lv J, Zhou Z, Tong L, Zhang S. Effects of heterogeneous ultrafine grain and strain rate on mechanical properties of CoCrNi medium entropy alloy. J Alloys Compd 2023;934:167791.
[46] Liang NN, Xu RR, Wu GZ, Gao XZ, Zhao YH. High thermal stability of nanocrystalline $FeNi_2CoMo_{0.2}V_{0.5}$ high-entropy alloy by twin boundary and sluggish diffusion. Mater Sci Eng, A 2022;848:143399.
[47] Cheng Q, Xu XD, Xie P, Han LL, He JY, Li XQ, et al. Unveiling anneal hardening in dilute Al-doped $Al_xCoCrFeMnNi$ ($x = 0$, 0.1) high-entropy alloys. J Mater Sci Technol 2021;91:270–7.
[48] Sun LX, Tao NR, Kuntz M, Yu JQ, Lu K. Annealing-induced hardening in a nanostructured low-carbon steel prepared by using dynamic plastic deformation. J Mater Sci Technol 2014;30:731–5.
[49] Wu X, Yang M, Yuan F, Wu G, Wei Y, Huang X, et al. Heterogeneous lamella structure unites ultrafine-grain strength with coarse-grain ductility. Proc Natl Acad Sci 2015;112(47):14501–5.
[50] Zhang R, Zhao S, Ding J, Chong Y, Jia T, Ophus C, et al. Short-range order and its impact on the CrCoNi medium-entropy alloy. Nature 2020;581:283–7.
[51] Chen X, Wang Q, Cheng Z, Zhu M, Zhou H, Jiang P, et al. Direct observation of chemical short-range order in a medium-entropy alloy. Nature 2021;592:712–6.